Escola de Camins
Escola Tècnica Superior d'Enginyeria de Camins, Canals i Ports
UPC BARCELONATECH

PROJECTE O TESINA D'ESPECIALITAT

Títol

Effects of turbulence and laser exposure on phytoplankton behavior

Autor

Miguel Calpe Linares

Tutor

Antonio Huerta Cerezuela

Departament

Departament de Matemàtica Aplicada III

Intensificació

Environmental Fluid Mechanics

Data

15 de Juny 2015

Effects of turbulence and laser exposure on phytoplankton behavior

M. Eng. Thesis

June, 2015

Environmental Fluid Mechanics Group
Civil, Environmental and Architectural Engineering Department
University of Colorado at Boulder
Boulder, United States

Escola Tècnica Superior d'Enginyeria de Camins, Canals i Ports de Barcelona
(ETSECCPB)
Universitat Politècnica de Catalunya
Barcelona, Spain

Author:
Miguel Calpe Linares
Balsells Fellowship

Supervisors:
Professor John P. Crimaldi
Postdoctoral Researcher Aaron True

Summary page

Phytoplankton are microscopic, unicellular and photosynthetic microorganisms that live in watery environments, both salty and fresh. They have an essential role in the earth's ecosystem as the foundation of the aquatic food web and contribute significantly to the global carbon budget. Spatial heterogeneity (or patchiness) in the distribution of organisms has important effects on ecological processes such as competition for nutrients, predation, and spread of epidemics. Some phytoplankton species have heterogeneous distributions within the flow, evading mixing and homogeneity driven by turbulence. Recent numerical studies attribute such heterogeneity to physical (turbulence) as well as biological (motility) processes; however the mechanisms that generate patchiness remain unclear. Here, we conducted the first laboratory experiments to study the interactions of marine phytoplankton and turbulent flows using an oscillating grid turbulence tank and laser imaging techniques.

The turbulence tank was built to generate homogeneous and isotropic turbulence in the center of the tank. At various operational states (grid frequency and stroke), different turbulence characterisctics can be achieved. The turbulence was quantified using particle image velocimetry (PIV). It is a non-intrusive method that computes the instantaneous velocity field within the flow using neutrally buoyant seeding particles. Phytoplankton cells were imaged using planar laser induced fluorescence (PLIF) using fluorescence properties of phytoplankton. The results obtained show, as numerical simulations predicted, that turbulence drives small scale patchiness in motile phytoplankton. However, the enhancement factor (patchiness intensity) obtained is lower than that computed numerically. A potential cause for this could be, the previous exposure may have affected phytoplankton behavior. In an effort to verify that the previous experimental techniques do not induce abnormal swimming behavior, a subset of experiments was performed to examine exposure effects. Assays were conducted in which phytoplankton were exposed to laser, turbulence and laser + turbulence. The motion of the cells was digitized using an image tracking software and kinematics of the cells was computed using MATLAB. Subsequently, the motion of the cells after each exposure assay was compared to their original motion (no exposure).

The results suggest that laser exposure has little effect on phytoplankton, while turbulence exposure disorientates the cells, making them slower and turn them more often. The cells recover their original motion after a certain period of time, showing that the effects of turbulence are not permanent rather temporary.

Acknowledgements

I would like to express my sincere gratitude to my three thesis supervisors, Associate Professor John P. Crimaldi (University of Colorado at Boulder, United States), Postdoctoral Researcher Aaron True (University of Colorado at Boulder, United States) for showing me the amazing world of fluid mechanics. Their fascination and expert advice has played a key role in the successful completion of this work. I am also grateful to Professor Antonio Huerta Cerezuela (Universitat Politècnica de Catalunya, Spain) for his continuous support and guidance during this thesis work.

I am indebted to Mr. Pete Balsells, Ms. Karey Sabol and Ms. Sharon Powers (Balsells Fellowship) who gave me the opportunity to do research at the University of Colorado at Boulder and to help me during my whole stay in United States. I would like also to express my sincere thanks to my lab-mates in Colorado for their friendship and help, Mr. Danny Birdsell, Mr. Kenneth Pratt, Mr. Jose Solis, Mr. Sachin Pandey, Ms. Aleah Sommers, Ms. Amy Piscopo, Mr. Greg Lackey, Mr. Masoud Arshadi and Mr. Farrockh Shoaei. In addition, I would like to thank specially the spanish community in Boulder, which has been also a great support during my stay.

Last but not least, my deepest gratitude to my whole family for being always available when I needed it. Especially, I would like to thank my mother Gloria Linares Díaz, my sister Cristina Linares Calpe and my uncle Josep Riu Ravetllat for teaching me that there are moments for working hard and others for playing hard.

Miguel Calpe Linares

"I think over again my small adventures.
My fears.
Those small ones that seemed so big.

For all the vital things
I had to get and to reach.

And yet there is only one great thing.
The only thing.

To live to see the great day that dawns
And the light that fills the world."

-Old Inuit Song-

Contents

List of Tables

List of Figures

1 Introduction and Purpose

Since phytoplankton are involved in a wide variety of natural phenomena, it is important to study their spatial distribution in the natural environment. Some phytoplankton species show heterogeneity in their spatial distributions under turbulent conditions. Both physical (turbulence) and biological (motility) conditions are thought to contribute to this heterogeneity. Recent studies have begun to reveal the physical-biological conditions responsible for enhanced patchiness in motile phytoplankton. An analytical model of gyrotactic motility in a simple vortical flow (Durham et al., 2011), followed by lab experiments and numerical simulations demonstrated spatial heterogeneity of live phytoplankton. However, quantitative experiments in realistic flows that mimic the turbulence conditions in the ocean have never been performed.

A collaborative effort between the University of Colorado and MIT aims to perform the first laboratory experiments examining patchiness in three-dimensional turbulence that mimics oceanic flow. The Environmental Fluid Mechanics Group at the University of Colorado, led by John P. Crimaldi, has been working for a long time with sophisticated laser-based methodologies to measure the entities transported by real three-dimensional turbulent flows (Crimaldi, 2008; Soltys and Crimaldi, 2011). The goal of this project is to study the spatial distribution of motile phytoplankton species, *Heterosigma akashiwo*. The cells will be exposed to homogeneous and isotropic turbulence using a miniature oscillating grid (MOG) tank. The turbulence within the tank will be quantified using particle image velocimetry (PIV). Then, the distribution of the cells will be imaged using planar laser induced fluorescence (PLIF) that exploits the fluorescence properties of phytoplankton cells to digitize cell location in space. Ultimately, images of cell distributions will be used to compare patchiness for different species in different flows.

An important part of the phytoplankton turbulence project, and the main focus of what will be presented here, is evaluating the potential effects of laser and turbulence exposure on phytoplankton swimming. Exposure assays will be conducted in which cell kinematics after each exposure will be compared to no exposure sample in order to quantify the effects on swimming behavior.

2 Literature Review

2.1 Phytoplankton Ecology

Phytoplankton are mostly microscopic, single-celled photosynthetic organisms that live suspended in water. They use light energy and inorganic nutrients such as nitrates, phosphates and sulfur to generate proteins, fats and carbohydrates. During this process, they take up carbon dioxide and release oxygen. Because they need light, phytoplankton live near the surface, where enough sunlight can penetrate to power photosynthesis. The thickness of this layer of the ocean, also known euphotic zone, varies depending on water clarity, but is at most limited to the top 200 to 300meters, out of an average ocean depth of 4000 meters.

Phytoplankton include species from the following divisions: cyanobacteria, silica-encased diatoms, dinoflagellates, green algae and chalk-coated coccolithophores. However, the two main classes of phytoplankton are dinoflagellates and diatoms. Dinoflagellates use a whip-like tail, or flagella, to move through the water and their bodies are covered with complex shells. Diatoms also have shells, but they are made of a different substance and their structure is rigid. Diatoms do not rely on flagella to move through the water and instead rely on ocean currents to travel through the water.

Figure 1: Different types of phytoplankton. The two main species of phytoplankton are dinoflagellates (motile) and diatoms (non-motile). The experiments have been performed with the dinoflagellate species *Heterosigma akashiwo*. (http://earthobservatory.nasa.gov/)

Importance on the food web

Phytoplankton are the foundation of the aquatic food web, the primary producers, feeding everything from microscopic, animal-like zooplankton to multi-ton whales. Small fish and invertebrates also graze on the plant-like organisms, and then those smaller animals are eaten by bigger ones. Some phytoplankton have a direct impact to humans and other animals. Dense blooms of some organisms can deplete oxygen in coastal waters, causing fish and shellfish to suffocate. Other species produce toxins that cause illness or death among humans and even whales that are either exposed to the toxins or eat shellfish that accumulate toxins. For instance, *Harmful algal blooms (HAB)* cause significant economic loss every year in the seafood industry and in tourist communities.

Importance on climate and carbon cycle

Through photosynthesis, phytoplankton consume carbon dioxide on a scale equivalent to forests and other land plants. Some of this carbon is carried to the deep ocean when phytoplankton die, and some is transferred to different layers of the ocean as phytoplankton are eaten by other creatures,

which themselves reproduce, generate waste, and die. Phytoplankton transfers about 10 gigatones of carbon from the atmosphere to the deep ocean every year. Even small changes in the growth of phytoplankton may affect atmospheric carbon dioxide concentrations, which would feed back to global surface temperatures.

2.2 Hetereogeneity Distribution (or patchiness) and Turbulence at Small Scales

Spatial heterogeneity, or "patchiness" of phytoplankton plays an essential role in the marine ecosystem by dictating the rate at which individual cells encounter each other and their predators (Durham et al., 2013). However, the mechanisms and causes that produce heterogenity remain still unknown. Many studies have observed that the distribution of phytoplankton in turbulent flows is more pachy in motile species than in non-motile species. It has been observed that the motile phytoplankton accumulate inside the vortices' cores, while non-motile phytoplankton remain randomly distributed. Consequently, motility is an indispensable component to generate spatial heterogeneity.

The motion of phytoplankton cells is called *gyrotaxis* and is resulted from two torques: a gravitational torque that stabilizes the cell, and a viscous torque due to fluid shear that acts to overturn it. Two parameters describe that motion, the gyrotactic timescale, **B**, the time perturbed cell takes to return to its equilibrium orientation, and **k** that measures how sensitive the cell is to shear.

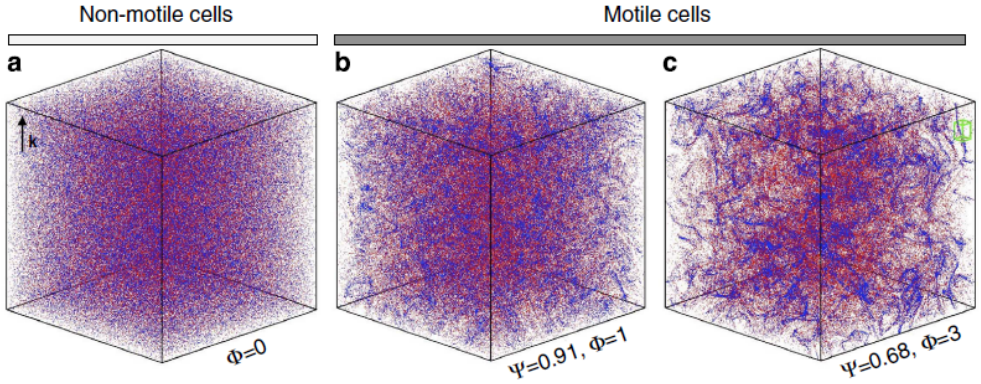

Figure 2: Spatial distribution for non-motile and motile species obtained by Direct Numerical Simulation (DNS). The cells with largest concentration (patches) are represented in *blue*, while the rest of the cells are represented in *red*. (Durham et al., 2013)

Recent studies (Durham et al., 2013) have performed direct numerical simulation (DNS) of homogeneus and isotropic turbulence with cells, whose motility was governed by gyrotaxis motion. The results ended up with patchiness in those distributions from motile phytoplankton, while non-motile phytoplankton were randomly distributed (see figure 2). The gyrotactic motility can be modeled by integrating the equation for the evolution of the swimming direction of a bottom-heavy spherical cell (Pedley and Kessler, 1992):

$$\frac{dp}{dt^*} = \frac{1}{2B}[k - (k \cdot p)p] + \frac{1}{2}(w^* \times p) \tag{1}$$

Where p is the unit vector along the swimming direction, $w^* = \nabla^* \times u^*$ is the fluid vorticity, t^* is time, $k = [0, 0, 1]$ is a unit vector in the vertical upwards direction, and B is the gyrotactic

reorientation timescale. The first term on the right side describes the tendency of a cell to remain aligned along the vertical direction, while the second term captures the tendency of vorticity to overturn the cell by imposing a viscous torque on it. Even though there are multiple scales of turbulence in the ocean, phytplankton cells only experiment shear at small scales, where energy is dissipated into heat by fluid viscosity. These scales can be assumed proportional to the Kolmogorov microscales:

$$\eta_K = (\frac{\nu^3}{\varepsilon})^{\frac{1}{4}} \sim 0.1 - 10\ mm \tag{2}$$

$$\omega_K = (\frac{\varepsilon}{\nu})^{\frac{1}{2}} \sim 0.01 - 10\ s^{-1} \tag{3}$$

Where η_K is the Kolmogorov length scale, ω_K is the Kolmogorov shear rate, ν the kinetic viscosity of seawater and ε the dissipation rate of kinetic energy. Then, two dimensionless parameters have been defined to control the cells' behavior, the swimming number, $\Phi = \frac{V_c}{V_k}$, and the stability number, $\Psi = B\omega_K$. The first parameter measures the swimming speed of the cell (V_c) relative to the Kolmogorov velocity ($V_k = \eta_k\omega_k$). The second parameter measures how unstable cells are to overturning by shear.

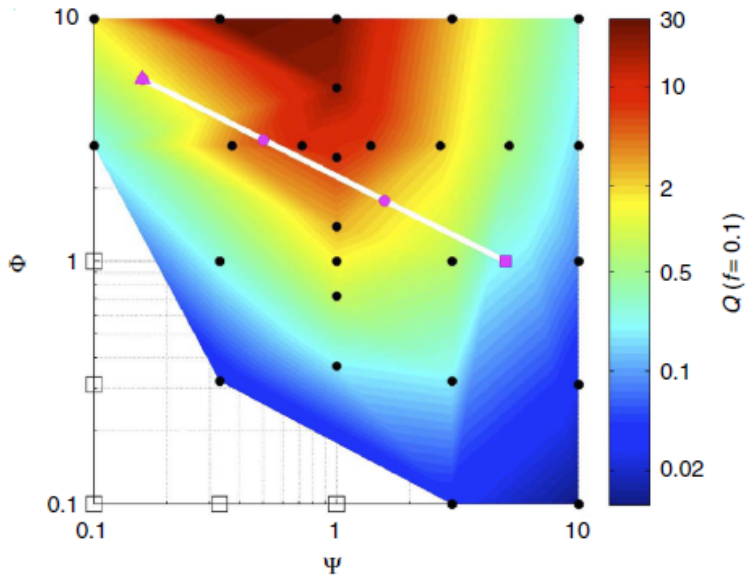

Figure 3: Phytoplankton distribution in the parameter space $[\Psi, \Phi]$. The cell concentration within patches, Q, increases with the non-dimensional swimming speed, Φ, and peaks at intermediate stability numbers, $\Psi \sim 1$. (Durham et al., 2013)

The figure 3 shows patch concentration enhancement factor (Q) depending on the cells' swimming speed and its unsteability. Fast swimming cells (large Φ) with intermediate stability ($\Psi \sim 1$) cause more concentrated patches. The factor Q is expressed as $Q = \frac{(C-C_P)}{C_M}$, where C is the mean cell concentration within patches, C_P is the mean cell concentration for a random distribution of cells and C_M is the overall cell concentration. The factor Q depends also on the fraction f of cells having the largest local concentration defined as patches.

Phytoplankton cells can only form patches if they swim across streamlines to converge within specific regions of the flow, in order to defy the homogenizing effect of turbulent dispersion. They can do so when their speed is large (Φ) and their stabilizing torque come to a balance between swimming direction that is highly unstable and isotropic ($\Psi \gg 1$) and one that is stable uniformly upwards ($\Psi \ll 1$). These conditions occur often in the ocean, phytoplankton swimming speeds, $V_c \sim 100 - 1000\ \mu m s^{-1}$, are larger than Kolmogorov velocities, $V_k \sim 300 - 1000\ \mu s^{-1}$, whereas the reorientation timescale generally spans the range $B \sim 1 - 10\ s$, which for typical dissipation rates, $\varepsilon = 10^{-8} - 10^{-6}\ m^2 s^{-3}$, and that corresponds to $\Psi \sim 1$. For the species used in the experiments, *Heterosigma akashiwo*, their swimming speeds are around 150 $\mu m s^{-1}$ and their reorientation timescale is approximately 10 s. Although they have intermediate stability, they are slower than Kolmogorov velocities, we expect thus lower heterogenity in our samples.

Either phytoplankton physiology (motile or non-motile) or flow conditions (turbulence) have enormous effect on spatial heterogeneity. Furthermore, patchiness has multiple consequences for phytoplankton, it may be advantageous for sexual reproduction, decreasing the distance between conspecific cells. On the other hand, it may be also detrimental because there is more competition for nutrients and enhances grazing by zooplankton. Besides the passive mechanisms driven by turbulence, phytoplankton can also regulate the parameters $[\Phi, \Psi]$ in order to increase encounter rates during a reproduction period or slow down their swimming speeds and decrease their predation risk. Regardless the mechanisms used, patchiness is a consequence of vertical phytoplankton migration.

3 Methods

The Phytoplankton culture was exposed to three different treatments: laser exposure, turbulence exposure and laser/turbulence exposure. The motion after each treatment was observed and compared to the motion of a non-exposure sample, also known as control.

First of all, the cell density of the sample was computed using the hemocytometer (or Neubauer chamber). Afterwards, the microorganims were exposed to different treatments and their motion were observed through the microscope. Several videos were recorded from microscope's screen. The trajectories of the cells were obtained from microscope videos using a particle tracking software (Hedrick Lab-North Carolina). Afterwards, MATLAB code was written in order to compute the kinematics of the particles: velocity, acceleration, head angle and variation of the head angle. Finally, the results were interpreted and plotted in order to provide a physical meaning to the output data.

3.1 Turbulence and Flow Quantification

3.1.1 Turbulence apparatus

The turbulence experiments were performed in a purpose-built plexiglass tank filled with the Phytoplankton culture. The dimensions of the tank are 7.5 $cm \times 7.5\ cm \times 16.5\ cm$; the figure 4 shows the tank used for running the experiments as a turbulence apparatus.

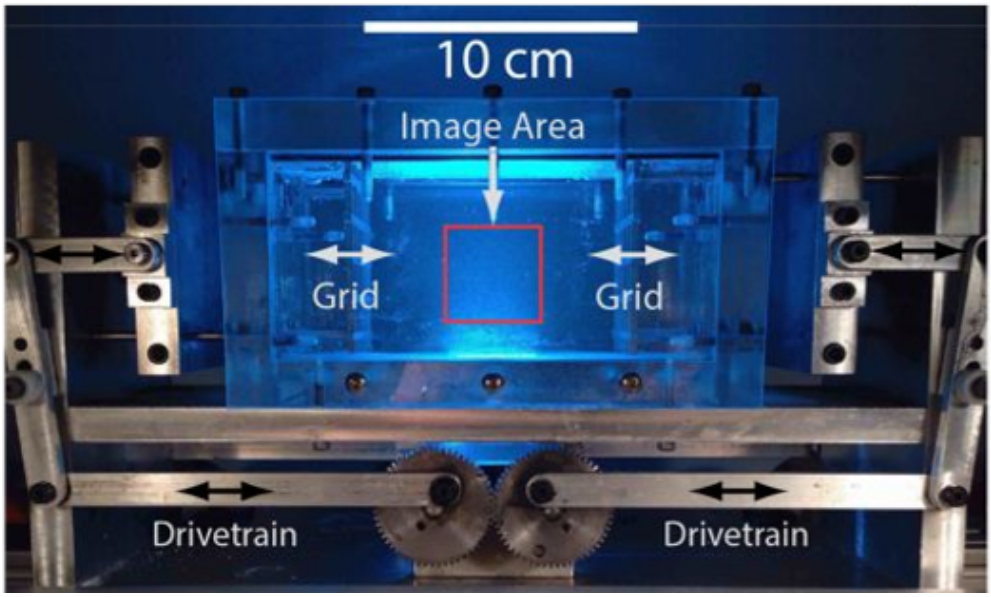

Figure 4: Miniature oscillating grid turbulence tank (MOG) used for the experiments. By controlling the stroke, $S(mm)$, and the frequency (Hz) of the tank, it is possible to obtain a wide range of turbulence intensities.

A pair of oscillating grids driven by electric motors with electronic speed controllers have been produced turbulence in the central portion of the tank that is approximately homogeneous and isotropic (Peters and Redondo, 1997; Srdic et al., 1996). Turbulent flow is *homogeneous* when the root mean square velocity fluctuations (rms) can be different between each other but each value is constant over the entire domain (invariant to axis translation). Furthermore, *isotropic*

turbulence implies even that the rms velocity fluctuations are independent of the direction of reference (invariant to axis rotation and reflection). In other words, homogeneous and isotropic turbulence must verify:

$$\sqrt{\overline{u^2}} = \sqrt{\overline{v^2}} = \sqrt{\overline{w^2}} \tag{4}$$

Where the $\overline{u^2}$ is the rms velocity fluctuation for x direction, $\overline{v^2}$ is the rms velocity fluctuation for y direction and $\overline{w^2}$ is the rms velocity fluctuation for z direction. The rms velocity fluctuations are the same at any point of the flow domain (homogeneous condition) and they must be the same also at any direction (isotropy condition).

Since the rms velocity fluctuations are the same, those flows have not any preference direction, therefore they do not have any mean flow. The presence of mean flow may introduce anisotropies in the turbulent velocity and pressure fields changing the turbulence pattern within the tank. In practical point of view, these flows are hypothetical because no actual flows can satisfy the conditions of isotropy. The best one can do is to generate flows in which conditions of isotropy are more or less approach. However, turbulent flows having these properties are in decaying state, that is the turbulence generated is not stationary, making hard to perform experiments on it. Posterior studies came up with an experimental set up which can generate nearly isotropic sustained (stationary) turbulence (Srdic et al., 1996).

The final design of our tank has been adopted from (Srdic et al., 1996), however the size of it has been scaled down. Since the present study is a preliminary part of a future greater project, an smaller tank was regarded enough, such that it requires less volume of phytoplankton and makes easier performing the experiments on it. It may be worth to mention that smaller sizes' tank can come up with secondary walls effects on the turbulence pattern, expecting thus different results as obtained in (Srdic et al., 1996), even changes on isotropic and homogeneous turbulence patterns.

3.1.2 Particle image velocimetry (PIV)

The turbulence in the tank was studied using the *particle image velocimetry (PIV)* technique (Grant, 1997). This method consists in introducing seeding particles into the flow, neutrally buoyant, and capturing consecutive images with a known frame rate. From knowledge of the position recorded at each image, as well as, the time between two images and the camera magnification, the velocity field of the fluid is obtained using a correlation method. The figure 5 shows the usual *PIV* scheme.

First of all, the seeding particles are selected to follow the accelerations within the flow with high accuracy, to scatter the light to form clear images and, to have relatively uniform size (Westerweel et al., 2012). The density of seeding particles within the tank has been computed, such that the number of particles per window is 10. The resolution of the SCMOS camera (*SCMOS imager, LAVISION technologies*) used for the experiments is 2160×2560 pixels. From the knowledge of the physical size of the image, the magnification factor can be computed as

$$\frac{15mm}{2560pixels} \approx 0.006\frac{mm}{pixel} \tag{5}$$

Since the frames are divided into small interrogation regions, typically with dimensions of 32×32

pixels, the physical size of one interrogation window is obtained as

$$32pixels \times 0.006\frac{mm}{pixel} = 0.1875\frac{mm}{window} \tag{6}$$

The thickness of the laser sheet is 1 mm, therefore the volume of an interrogation window is

$$Volume = (0.1875mm)^2 \times 1mm = 0.035\frac{mm^3}{window} \tag{7}$$

Regarding that 10 particles per interrogation window is enough to perform the PIV, the number of particles that should be within a window volume is

$$10\frac{particles}{window} \times \frac{window}{0.035mm^3} = 285.71\frac{particles}{mm^3} \tag{8}$$

$$285.71\frac{particles}{mm^3} \times \frac{10^3mm^3}{1cm^3} = 285710\frac{particles}{cm^3} \tag{9}$$

The density of the seeding particles used for the PIV is $2.685 \times 10^8 \frac{particles}{g}$. Considering also the results from the equations (**??**) and (9), the total density of seeding particles needed for performing the PIV measurements is expressed as:

$$285710\frac{particles}{cm^3} \times 928.125cm^3 \times \frac{1}{2.685 \times 10^8 \frac{particles}{g}} = \mathbf{987.6\ mg} \tag{10}$$

The imaging of the sample was carried out using a high resolution camera with high frame rate, 30 frames per second (fps). The illumination was provided by a laser, shaped into a planar sheet using a cylindrical lens. The laser beam expands through the lens since its focal length is negative, $f = -20mm$. Furthermore, a short laser pulse was used in order to freeze the particle images at a specific time (see figure 5).

Once a sequence of two light pulses was recorded, the images were divided into small regions called interrogation windows (IW), the dimensions of which determine the spatial resolution of the measurement. The interrogation windows can be adjacent to each other, or more commonly, have partial overlap with their neighbors that will increase the spatial resolution. Then, a cross correlation procedure is performed on two interrogated regions, seeking for the average displacement vector (dx, dy) which matches the maximum correlation (signal peak). The cross correlation method was used, basically, as a method of estimating the degree, to which two intensity series are correlated.

Considering two intensity distribution signals $x(i)$ and $y(i)$ of the same interrogation window at different time series, the cross correlation function at lag d is defined as:

$$r(d) = \frac{\sum_i [x(i) - \bar{x}] \times [y(i) - \bar{y}]}{\sqrt{\sum_i [x(i) - \bar{x}]^2} \times \sqrt{\sum_i [y(i) - \bar{y}]^2}} \tag{11}$$

The functions $x(i)$ and $y(i)$ represent the intensity signals, whereas $\bar{x}$ and $\bar{y}$ are the intensity mean of the interrogation windows and $r(d)$ is the cross correlation function at the position shift d.

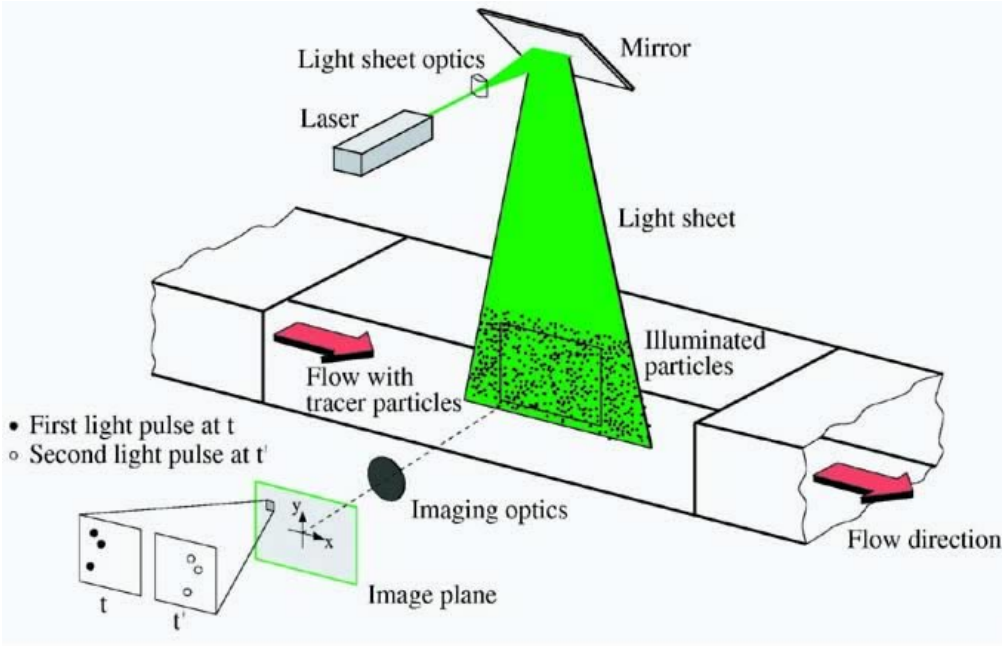

Figure 5: Experimental set up for PIV technique. The seeding particles are illuminated by a laser sheet. The CCD camera captures images with specific time rate. From the knowledge of the time between two exposures and the position of the particles, the instantaneous velocity field can be obtained for each image. (http://aim2.dlr.de/)

The denominator in the expression above serves to normalize the correlation coefficients such that $-1 \leq r(d) \leq 1$, the bounds indicating maximum correlation and 0 indicating no correlation. To relieve the heavy computation burden, *Fast Fourier Transforms (FFT)* were used to speed up the cross correlation calculations, since doing so would reduce the number of computational operations for each interrogated region from N^4 to $N^2 log_2 N$ (Willert and Gharib, 1991).

There are different methods for finding the position shift with maximum correlation (signal peak). The three methods more common used are: *Peak centroid*, *Parabolic* and *Gaussian*. The first method is strongly biased the displacements measurements towards an integer values, creating a peak-locking effect on processed data. The second and third approaches, which curve-fitted the maximum peak and its two side-peaks, are more robust. The PIV technique was performed using *Gaussian* approach. Since the particle images are well aproximated by Gaussian intensity distributions, when correlated also result in a Gaussian intensity distribution. Its estimation is therefore much better using a Gaussian curve fit, rather than a parabolic curve fit.

Considering the average displacement vector at each interrogation window, and given the time interval between two laser pulses and the image magnification from camera calibration, the projection of the local flow velocity vector onto the plane of the light sheet can be deduced. In order to quantify the tubulence within the tank, turbulent kinetic energy dissipation rate has been computed from definitions of (Hinze, 1975).

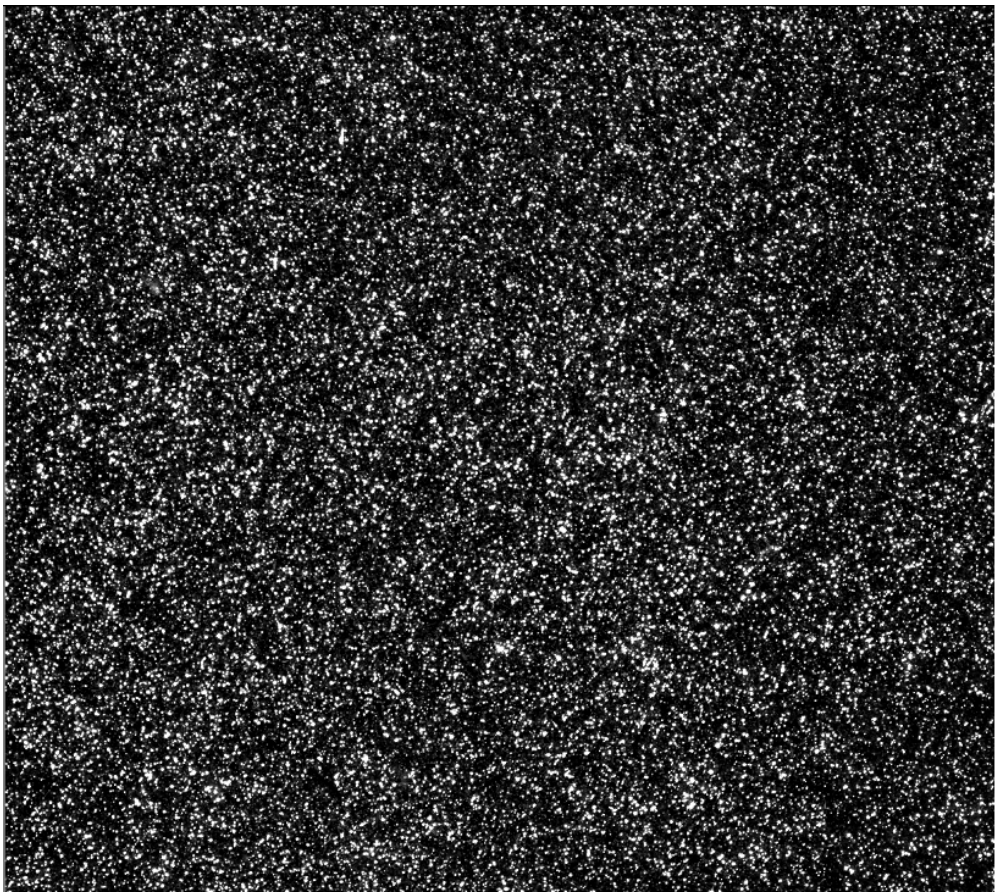

Figure 6: Seeding particles in the tank. The seeding particles are represented in white. They have different brightness as they are located at different depth of field. By setting the intensity parameter, we just consider those particles that are at the central part of the depth of field.

$$\varepsilon = \nu \overline{\frac{\partial u_j}{\partial x_i}\left(\frac{\partial u_i}{\partial x_j} + \frac{\partial u_j}{\partial x_i}\right)} \tag{12}$$

Since the turbulence generated in the tank is homogeneous, the dissipation rate is expressed as:

$$\varepsilon = \nu \overline{\frac{\partial u_j}{\partial x_i}\frac{\partial u_j}{\partial x_i}} = \nu \frac{1}{2}\overline{\left(\frac{\partial u_j}{\partial x_i} - \frac{\partial u_i}{\partial x_j}\right)\left(\frac{\partial u_j}{\partial x_i} - \frac{\partial u_i}{\partial x_j}\right)} \tag{13}$$

In isotropic turbulence the relation is simplified to the following two-dimensional form:

$$\varepsilon = 6\nu[\overline{(\frac{\partial u_1}{\partial x_1})^2} + \overline{(\frac{\partial u_1}{\partial x_2})^2} + \overline{\frac{\partial u_1}{\partial x_2}\frac{\partial u_2}{\partial x_1}}] = 15\nu\overline{(\frac{\partial u_1}{\partial x_1})^2} = 7.5\nu\overline{(\frac{\partial u_1}{\partial x_2})^2} \tag{14}$$

The accuracy of the estimated dissipation rate depends on the image area size, the interrogation area size and the velocity measurement error. If the image and the interrogation area sizes are too large, under-sampling phenomena occur. If the image and interrogation area sizes are too small, there is more noise in the results (Saarenrinne and Piirto, 2000). Furthermore, other important

Curve-Fitting Function	Three-point Estimator
Peak centroid	
$f(x) = \frac{1st\ order\ moment}{2nd\ order\ moment}$	$x_0 = \frac{(i-1)R_{(i-1,j)}+iR_{(i,j)}+(i+1)R(i+1,j)}{R_{(i-1,j)}+R_{(i,j)}+R_{(i+1,j)}}$
	$y_0 = \frac{(j-1)R_{(i,j-1)}+jR_{(i,j)}+(j+1)R_{(i,j+1)}}{R_{(i,j-1)}+R_{(i,j)}+R_{(i,j+1)}}$
Parabolic	
$f(x) = A(x_0 - x)^2$	$x_0 = \frac{R_{(i-1,j)}-R_{(i+1,j)}}{2R_{(i-1,j)}-4R_{(i,j)}+2R_{(i+1,j)}}$
$+B(x_0 - x) + C$	$y_0 = \frac{(R_{(i,j-1)}-R_{(i,j+1)}}{2R_{(i,j-1)}-4R_{(i,j)}+2R_{(i,j+1)}}$
Gaussian	
$f(x) = Aexp[\frac{-(x_0-x)^2}{B}]$	$x_0 = \frac{lnR_{(i-1,j)}-lnR_{(i+1,j)}}{2lnR_{(i-1,j)}-4lnR_{(i,j)}+2lnR_{(i+1,j)}}$
	$y_0 = \frac{(lnR_{(i,j-1)}-lnR_{(i,j+1)}}{2lnR_{(i,j-1)}-4lnR_{(i,j)}+2lnR_{(i,j+1)}}$

Table 1: Three-point estimators used to achieve subpixel resolution. The indices (i,j) correspond to the spatial location of the maximum location of the correlation valuewithin the correlation domain. It was used *Gaussian* approximation function for running the experiments.

differenciable quantities, such as vorticity and strain rate, can be computed from the velocity field. The vorticity and strain rate are both consequence of the deformation tensor, which is:

$$\frac{d\overrightarrow{U}}{d\overrightarrow{X}} = \begin{bmatrix} \frac{du}{dx} & \frac{dv}{dx} & \frac{dw}{dx} \\ \frac{du}{dy} & \frac{dv}{dy} & \frac{dw}{dy} \\ \frac{du}{dz} & \frac{dv}{dz} & \frac{dw}{dz} \end{bmatrix} \tag{15}$$

The vorticity vector is expressed as a function of the velocity field of the fluid (equation 16). In two dimensions, the vorticity is the sum of the angular velocities of any pair of mutually-perpendicular, infinitesimal fluid lines passing through the point in question.

$$\overrightarrow{W} = \nabla \times \overrightarrow{U} \tag{16}$$

Since the vorticity and strain rates fields cannot be directly measured, differentiation schemes must be used to derive these quantities. Such schemes, however, are susceptible to errors resulting from different grid spacing as well as noise within the velocity data. It is therefore important to be able to study and characterize various differentiation schemes in order to ascertain their performance.

Scheme	Implementation	Accuracy	Uncertainty
Forward difference	$(\frac{df}{dx})_{i+1/2} \approx \frac{f_{i+1}-f_i}{\Delta X}$	$O(\Delta X)$	$\approx 1.41\frac{\varepsilon_u}{\Delta X}$
Backward difference	$(\frac{df}{dx})_{i-1/2} \approx \frac{f_i-f_{i-1}}{\Delta X}$	$O(\Delta X)$	$\approx 1.41\frac{\varepsilon_u}{\Delta X}$
Center difference	$(\frac{df}{dx})_i \approx \frac{f_{i+1}-f_{i-1}}{2\Delta X}$	$O(\Delta X^2)$	$\approx 0.7\frac{\varepsilon_u}{\Delta X}$
Richardson extrapolation	$(\frac{df}{dx})_i \approx \frac{f_{i-2}-8f_{i-1}+8f_{i+1}-2f_{i+2}}{12\Delta X}$	$O(\Delta X^3)$	$\approx 0.95\frac{\varepsilon_u}{\Delta X}$
Least squares	$(\frac{df}{dx})_i \approx \frac{2f_{i+2}+f_{i+1}-f_{i-1}-2f_{i-2}}{10\Delta X}$	$O(\Delta X^2)$	$\approx 1\frac{\varepsilon_u}{\Delta X}$

Table 2: First order differential operators for data spaced at uniform ΔX intervals along the X-axis.

The accuracy of each scheme is defined as the truncation error associated with each scheme, and the uncertainty of each scheme is dependent on the velocity measurement uncertainty within the velocity field. Table 2 suggests that the forward and backward differentiation schemes would perform poorly, as both their accuracies and uncertainties are the highest.

3.2 Phytoplankton Culturing and Observation Techniques

3.2.1 Microorganism cultures

The phytoplankton species used for running the experiments is the motile dinoflagellate *Heterosigma akashiwo*, also known as *Red Tide*. It is a swimming alga relatively small, ranging in size from 18μm to 34μm. As it is said above, Heterosigma akashiwo species have two flagella; the leading flagellum allows the cell to move within the fluid with a certain direction **p**, whereas the second flagellum has less clear function on its motion (Hara and Chihara, 1987). Nevertheless, the second flagellum introduces a torque to the rotation of the cell, in addition to the torque from the center of gravity offset, and the viscous torque due the rotation of the cell within viscous media. This set of torques together end up with a helical motion, reducing the ability of cells to swim vertically upwards, and consequently reduce horizontal dispersal due to differential advection by the flow (Bearon, 2000).

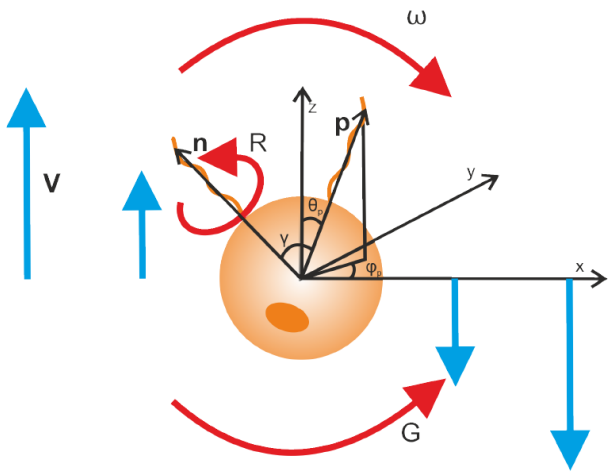

Figure 7: Torques acting on spheroidal cell. The gravitational torque, G, stabilizes the cell, whereas the shear torque, W, due to the viscous forces in the fluid and acts destabilizing the cell. (Bearon, 2000)

3.2.2 Observation and cell tracking and computation of kinematics

The observation of the cells was carried out using a Digital Binocular Compound microscope (*MD827S30 series, OMAX*). Afterwards, the microscope was connected to the computer and it was recorded the motion of Phytoplankton after exposure. For each exposure assay, it was recorded three videos to have enough trajectories to compute the kinematics of the particles. The figure 8 shows a caption of a video recorded during the experiments. The cells are in red and were recorded at room temperature during 3 minutes.

The tracking of the phytoplankton cells was done using *DLTdv3*, an open MATLAB code from Hedricks Laboratory (University of North Carolina). The mentioned code computes the position

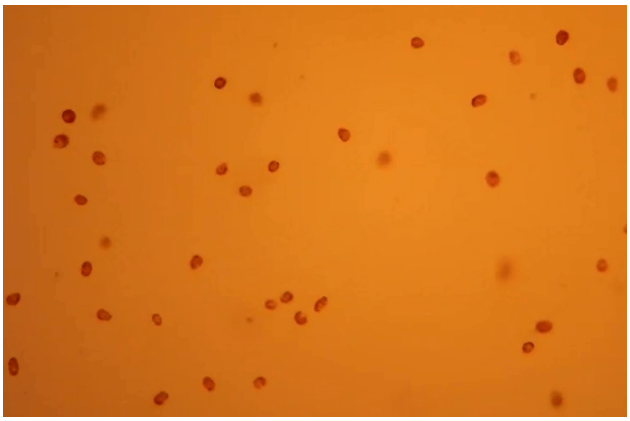

Figure 8: Microscope caption of phytoplankton species *Heterosigma akashiwo*. The cells are represented in red, the caption was taken at room temperature and without any laser or turbulence exposure.

of the cells over the time and writes down the ouptut data. To compute the position of the cells, an array of pixels is considered within the cell in a certain frame *n*. Using coloration patterns, the code identifies the new position of the cell in frame *n+1*. Moreover, cross-correlation method is used to match accurately the position of the cells from frame n with cells in frame *n+1*. Finally, a reconstruction operation is required to map pixel coordinates $[u, v]$ to two-dimensional coordinates $[x, y]$ (Hedrick, 2008).

A MATLAB code was written to compute the kinematics of the cells from the tracking data. The input are the position of the cells and the code computes the velocity, acceleration, head angle and variation of the head angle for each treatment, as well as statistical parameters such as mean and standard deviation. Having the position of the cell at each time, the 2D displacement can be computed as:

$$\Delta X = X_{n+1} - X_n \tag{17}$$

$$\Delta Y = Y_{n+1} - Y_n \tag{18}$$

where X_{n+1} and Y_{n+1} are the position of the cell at the frame $n+1$, X_n and Y_n are the position of the cell at the fram n, and ΔX and ΔY are the displacements in both directions respectively. From the knowledge of the frame rate, the velocity of cell can be obtained as:

$$V_x = \frac{\Delta X}{t} \tag{19}$$

$$V_y = \frac{\Delta Y}{t} \tag{20}$$

where V_x and V_y are the velocity components in x and y directions, and t is the time between two consecutive frames. The velocity value of the cell is thus:

$$V = \sqrt{(V_x)^2 + (V_y)^2} \tag{21}$$

The acceleration of the cell is computed as the other kinematic parameters from above:

$$a_x = \frac{\Delta V_x}{t} \tag{22}$$

$$a_y = \frac{\Delta V_y}{t} \tag{23}$$

$$a = \sqrt{(a_x)^2 + (a_y)^2} \tag{24}$$

In addition to the velocity of the cells, the cells' head angle and its variation over time are relevant information of the motion of phytoplankton. A large change in their head angle may be produced by the turbulence or laser exposure and it is required to be analyzed. The head angle of phytoplanton cells is computed as:

$$\theta_n = \arctan(\frac{\Delta X_n}{\Delta Y_n}) \tag{25}$$

$$\Delta\theta_n = \theta_{n+1} - \theta_n \tag{26}$$

where θ_n is the head angle at frame n, while $\Delta\theta_n$ is the head angle variation between the frames n and $n+1$.

3.3 Phytoplankton Turbulence Experiments

3.3.1 Microscale laser-based imaging system

Laser exposure assay was carried out using the same method as for phytoplankton visualization, planar laser-induced fluorescence (PLIF) (Crimaldi, 2008). A 50μm light sheet from an argon-ion laser illuminates a 2 $cm \times 2$ cm measurement region, inducing chlorophyll to fluorescence from phytoplankton residing in the sheet, permitting the location and distribution of individual cells to be quantitatively imaged using a scientific camera.

Planar Laser-Induced Fluorescence (PLIF)

PLIF is a non-intrusive technique for measuring scalar concentration in flows using fluorescence properties (Crimaldi, 2008). Fluorescence is the emission of light by a substance that has absorbed light or other electromagnetic radiation. An electron in the ground level (low energy) absorbs a photon and it is transferred to excited energy level (high energy). This electron emits then the photon while returning to the lower energy level, which is seen as a fluorescence signal (see figure 9). In most cases, the emitted light has a longer wavelength, and therefore lower energy, than the absorbed radiation.

Phytoplankton cells have fluorescent properties since they contain chlorophyll *a*. Phytoplankton cells are excited using laser sheet and they absorb a portion of the excitation energy. Simultaniously they re-emit a portion of the absorbed energy as fluorescence. The fluorescence can be related to the cell's concentration. The combination of chlorophyll *a* and other cellular components inside phytoplankton cells have a maximum absorption near 440 nm and maximum fluorescence at 685 nm (Leeuw et al., 2013). This relation between local fluorescence F, local concentration C and local excitation intensity I is given by:

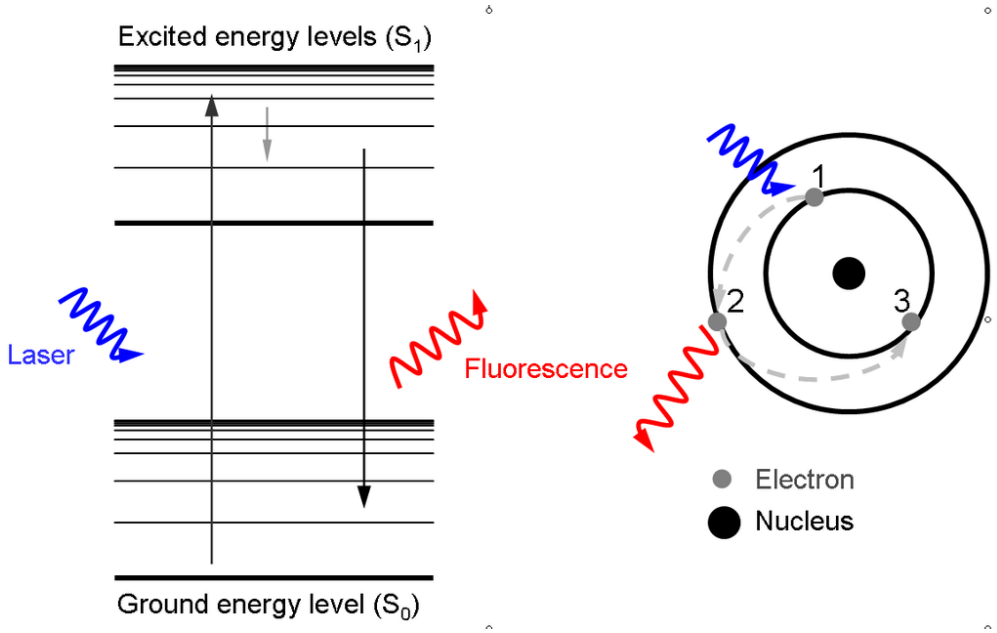

Figure 9: Phenomenon of fluorescence. It occurs when an orbital electron of a molecule, atom or nanostructure relaxes to its ground state by emitting a photon of light after being excited to a higher quantum state by some type of energy. (http://commons.wikimedia.org)

$$F \propto C \frac{I}{1 + \frac{I}{I_{sat}}} \tag{27}$$

Where I_{sat} is the saturation intensity for the phytoplankton cells, and it occurs when the exitation rate exceeds the fluophore deactivation rate. However, if the excitation is "weak", $I \ll I_{sat}$, the relation becomes linear:

$$F \propto CI \tag{28}$$

The relation from above provides local cell concentration from the fluorescence measurement (F). However, the local excitation intensity (I) can vary spatially and temporally along the ray path. The change of excitation intensity (dI) of a ray due to absorption (ϵ) crossing a solution with concentration (C) can be represented by the Beer-Lambert law as:

$$\frac{dI}{I} = -\epsilon C dr \tag{29}$$

So that, the local intensity of a ray passing from r_0 to r_1 with a variable concentration field is:

$$I(r_1) = I(r_0) exp[-\epsilon \int_{r_0}^{r_1} C(r) \mathrm{dr}] \tag{30}$$

Systems are called "optically thin" if the attenuation is negligible along the path from r_0 to r_1:

$$\epsilon \int_{r_0}^{r_1} C(r)\mathrm{dr} \ll 1 \tag{31}$$

Furthermore, fluorescence theory shows that always the energy emitted as fluorescence is less than absorbed energy. The quantum efficiency (ϕ) is the ratio of light energy emitted to energy absorbed, hence it is always equal or less than 1. Therefore, the fluorescence emitted by a prismatic volume oriented along the the axis of the incident excitation ray with volume $dV = drdA$ can be measured as:

$$dF = -\phi dIdA = \phi\epsilon ICdV \tag{32}$$

For the PLIF experiments, a radial laser sheet is used to illuminate the sample region. As PIV technique, the laser sheet is generated by passing a narrow laser beam through cylindrical lens located at the origin (see figure 10). The intensity distribution within laser sheet will be:

$$I(r, \theta, z) = Pa(r, \theta)f(r)g(\theta)h(z) \tag{33}$$

Where P is the power of the laser beam, $a(r, \theta)$ is the attenuation along the laser sheet due to phytoplankton absorption and $f(r)g(\theta)h(z)$ are the unattenuated spatial intensity distribution. The camera will image fluorescence from a right prismatic volume (dV), that is the right projection of a small area, $dA = rdrd\theta$, across the width of the sheet. The integration of the equations 32 and 33 over the sheets' width ends up with:

$$F = \phi\epsilon Pa(r, \theta)f(r)g(\theta)C\delta A \tag{34}$$

where C is the averaged concentration over the small volume dV. Then, the fluorescence intensity imaged at any pixel location (i, j) is thus:

$$I_F(i, j) = \beta(i, j)\frac{F}{\Delta A} = \alpha(i, j)a(r, \theta)C \tag{35}$$

$$\alpha(i, j) = \beta(i, j)\phi\epsilon Pf(r)g(\theta) \tag{36}$$

where $\beta(i, j)$ is the fraction of fluorescence received by the camera optics at a particular pixel, and $\alpha(i, j)$ is the collection of concentration. So that, the concentration of phytoplankton can be determined as:

$$C = [\alpha(i, j)a(r, \theta)]^{-1}I_F \tag{37}$$

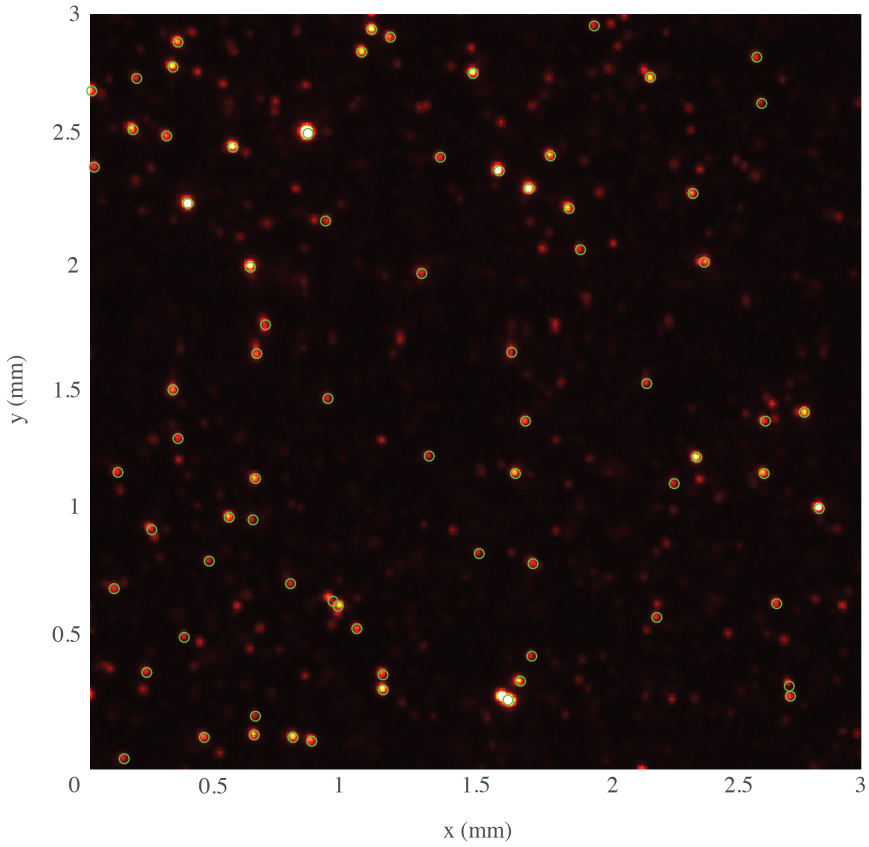

Figure 10: Imaging phytoplankton cells using PLIF technique. The cells with green circles are those detected by the software through intensity identification.

4 Results and Discussion

4.1 Turbulence Characteristics (PIV)

The experiments for the present project have been performed using image pairs (double-exposure) at 15 Hz, where the time between image pairs (dt) has been iteratively optimized to obtain a particle displacement from 5 to 10 pixels. Pre-processing of the images has been carried out using the same software as for PIV technique (*LabVision*) for background minimum subtraction (dark response and correction of reflections) in order to facilitate cell identification as well as cross-correlation peak finding.

The turbulence characteristics have been computed for different values of grid displacements (mm) and oscillation frequencies (Hz). The table 3 summarizes the turbulence parameters obtained such as mean turbulence intensity, mean of turbulent kinetic energy dissipation rate (TKE) as well as Kolmogorov microscale, velocity scale and shear rate. These parameters have been time and spatial averaged in a 1cm by 1cm box at the center of the tank volume. The table 3 shows also that for larger grid amplitude and larger frequencies, the turbulence apparatus generates larger turbulence and thus higher kinetic energy is dissipated in the process. However, dissipation rates

are lower than we expected, dissipation as a $f(stroke, frequency)$ is decently close to expected form the grid turbulence literature.

From the PIV technique has been computed either instantaneous velocity fields (represented as streamlines at the figure 11) and vorticity field (see figure 12). The figure 11 shows an instantaneous velocity field from the PIV experiment performed in the laboratory. The *blue* lines represent those seeding particles with low velocity, whereas *red* particles are those with high velocity. The direction of the flow is represented by arrays.

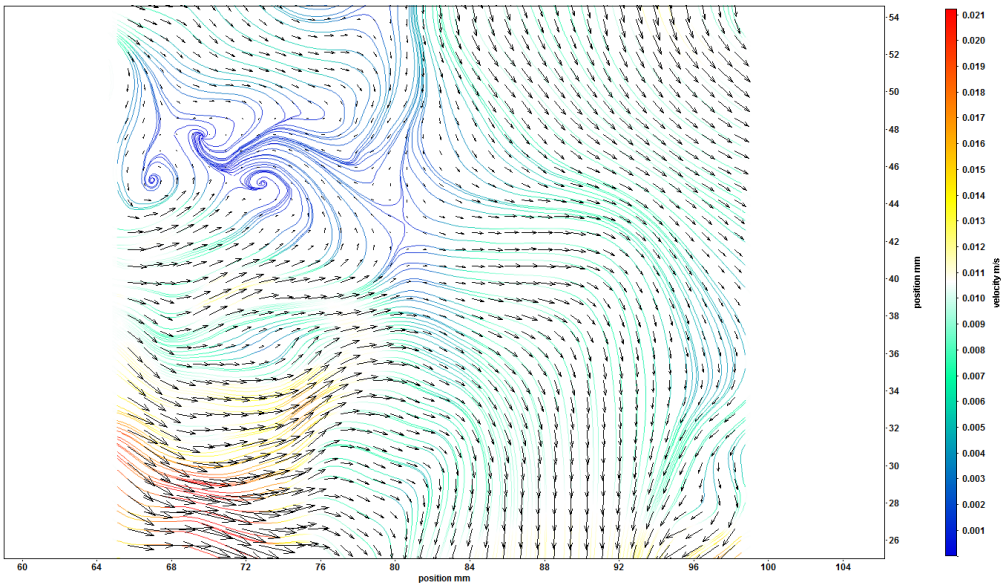

Figure 11: Instantaneous vector field and streamlines. The particles with high velocity are represented in *red*, whereas those particles with low velocity are represented in *blue*.

Full displacement Stroke (mm)	**Oscillation frequency (Hz)**	**Mean turbulence intensity (mm/s)**	**Mean TKE dissipation rate (mm^2/s^3)**	**Kolmogorov microscale (mm)**	**Kolmogorov velocity scale (mm/s)**	**Kolmogorov shear rate (s^{-1})**
15	0.5	1.983	0.002	4.678	0.214	0.046
15	1	4.435	0.007	3.462	0.289	0.083
15	2	5.773	0.010	3.184	0.314	0.099
15	4	6.795	0.012	3.045	0.328	0.108
20	4	8.103	0.016	2.815	0.355	0.126

Table 3: Summary of turbulence characteristics for various grid stroke and frequency combinations.

The figure 12 represents an instantaneous vorticity field obtained from the post-processing PIV experiment. As we expected, those particles with larger cross velocity gradients (zones represented in *red*), they do have more tendency to rotate and thus larger vorticity values. The spots closer to the grids have more vorticity than the central portion of the tank (zone represented in *blue*).

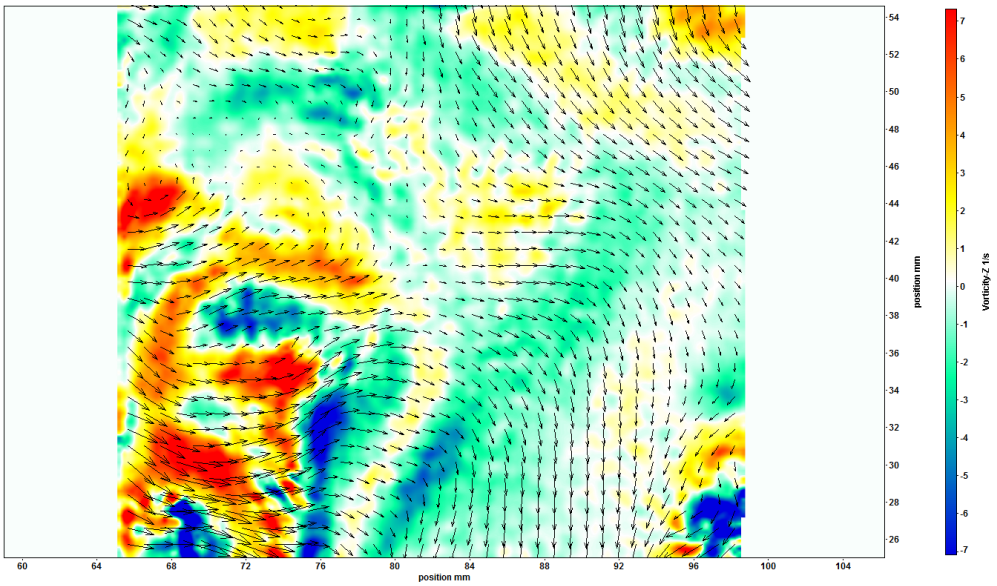

Figure 12: Instananeous vorticity field W_z. The zones colored in *red* have larger velocity than those colored in *blue*.

4.2 Exposure Assays and Cell Kinematics

The motion of the microorganisms is not affected by laser exposure. However, the turbulence exposure changes the behavior of the phytoplankton, disorientating them and thus making them slower. It has been observed that they recover their motion after turbulence exposure. The table 4 summarizes the kinematics of the microorganisms for each treatment.

		Control	**Laser**	**Turbulence (Just after)**	**Turbulence (190 min)**	**Laser and turbulence**
Velocity ($\frac{mm}{s}$)	**Mean**	0.086876	0.075500	0.007477	0.076535	0.025598
	Std	0.024	0.023	0.007	0.023	0.008
Angle variation (°)	**Mean**	35.067	35.291	73.418	44.559	38, 311
	Std	14.052	16.880	22.679	22.637	9.067

Table 4: Exposure assays results.

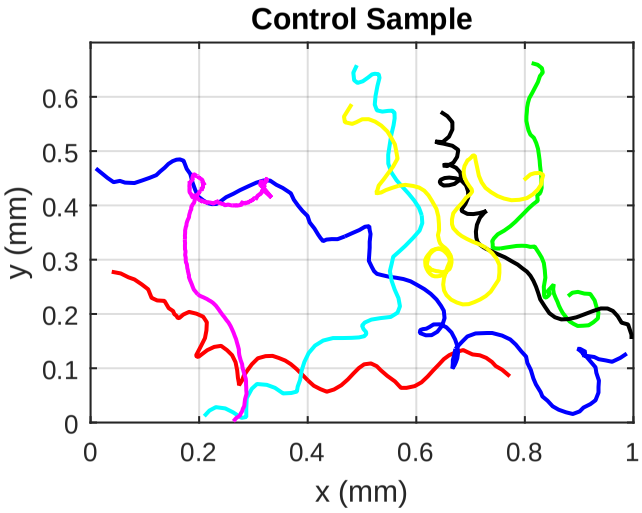
Control Sample
y (mm)
x (mm)
0
0.1
0.2
0.3
0.4
0.5
0.6
0.2
0.4
0.6
0.8
1

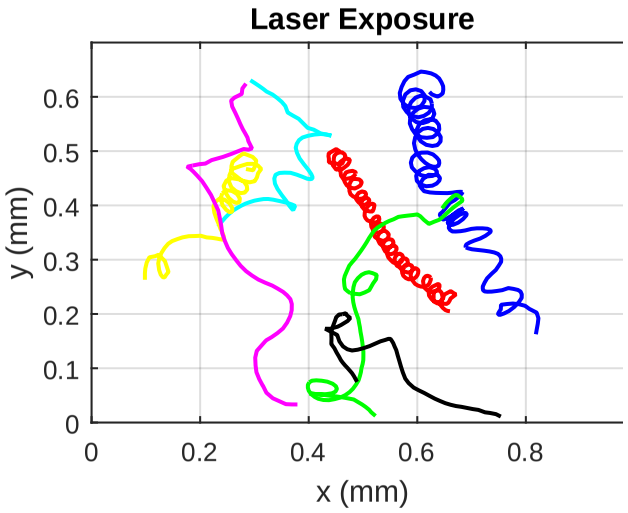
Laser Exposure
y (mm)
x (mm)
0
0.1
0.2
0.3
0.4
0.5
0.6
0.2
0.4
0.6
0.8

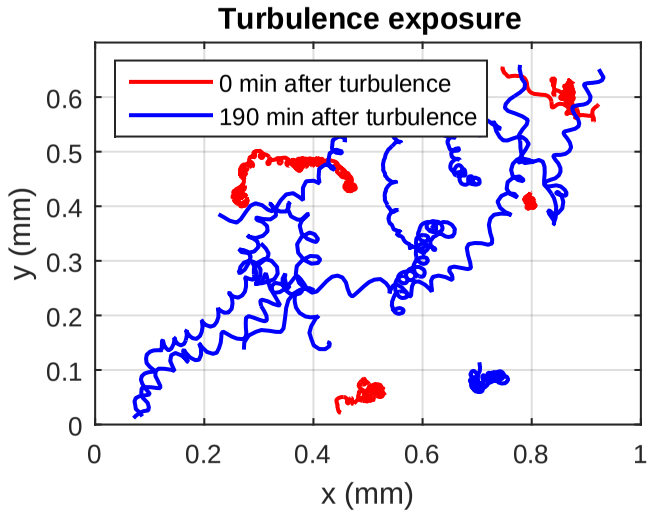
Turbulence exposure
0 min after turbulence
190 min after turbulence
y (mm)
x (mm)
0
0.1
0.2
0.3
0.4
0.5
0.6
0.2
0.4
0.6
0.8
1

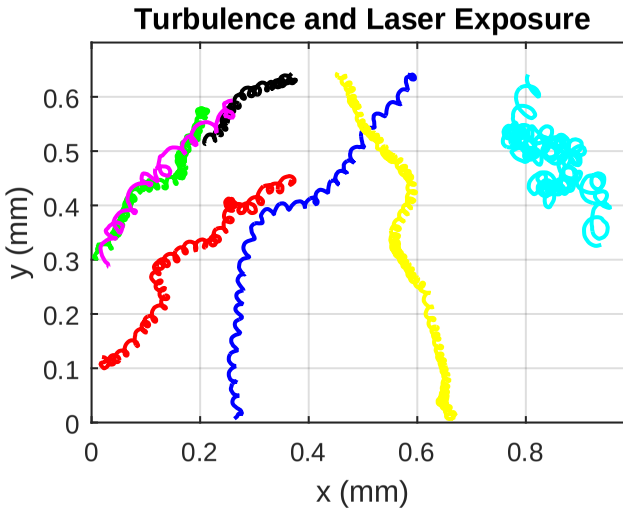
Turbulence and Laser Exposure
y (mm)
x (mm)
0
0.1
0.2
0.3
0.4
0.5
0.6
0.2
0.4
0.6
0.8

Turbulence Exposure

Since Phytoplankton microorganisms live in a turbulent environment such as oceans and lakes, it is worth to focus deeper into the effects of turbulence flows on Phytoplankton cells. Just after turbulence exposure, the velocity mean is one order less than the control sample. While the cells have a linear velocity close to zero (small mean velocity), they spin around themselves and therefore, they have a large head angle variation (large angular velocity).

		Control	**Turbulence (Just after)**	**Ratio (no units)**
Velocity ($\frac{mm}{s}$)	**Mean**	0.086876	0.007477	0.086
	Std	0.024	0.007	(V_{190min}/V_c)
Angle variation (°)	**Mean**	35.067	73.418	2.09
	Std	14.052	22.679	($\Delta\theta_{190min}/\Delta\theta_c$)

Table 5: Exposure assays results: Just after turbulence exposure

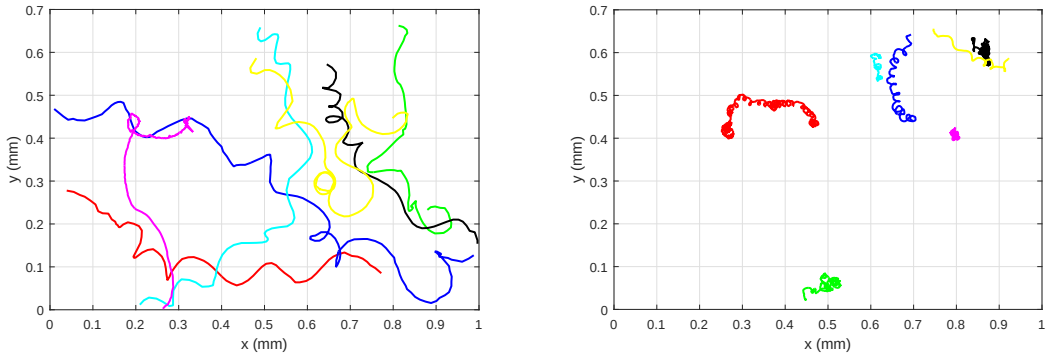

Figure 14: Trajectories control sample (*left plot*) and just after turbulence exposure (*right plot*)

With regard to the variability of the data obtained, the velocity of those cells from the control sample have a larger standard deviation than those tracked just after turbulence exposure. It is due to the randomness of the cells behavior, the first ones move randomly through the flow while the second ones have lost already this randomless as they have been disorientated by turbulence exposure (see figure 14). However, the variability on head angle variation data is larger in those cells exposed to turbulence than those from the control sample. As it is shown at the figure from below (see figure 14), after turbulence exposure each cell has different grade of disorientation, some of them will have a great angle variation, whereas other cells have smaller head angle variation. There may be two explanations: either one hand, the cells have different resilience of turbulence or since they are located in different points of the flow, the turbulence affect thus differently to each cell. Anyway, this variability ends up with a large standard deviation of the head angle variation parameter.

The cells have been tracked 190 minutes after turbulence exposure in order to study if either they recover their motion over the time or they remain disorientated. The table 6 shows that either velocity ratio and angle variation ratio are close to one, so that phytoplankton cells recover their motion after a certain period of time. It may be interesting to study how long it does take to the cells to recover their original motion for each turbulence intensity.

		Control	**Turbulence (190 min)**	**Ratio (no units)**
Velocity ($\frac{mm}{s}$)	**Mean**	0.086876	0.076535	0.88
	Std	0.024	0.023	(V_{190min}/V_c)
Angle variation (°)	**Mean**	35.067	44.559	1.27
	Std	14.052	22.637	($\Delta\theta_{190min}/\Delta\theta_c$)

Table 6: Exposure assays results: 190 minutes after turbulence exposure.

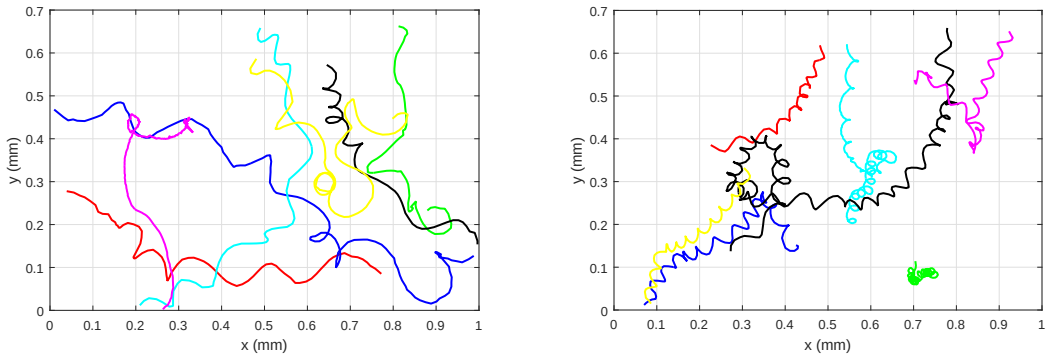

Figure 15: Trajectories control sample (*left plot*) and 190 minutes after turbulence exposure (*right plot*).

5 Conclusions and Future Recomendations

Indeed, laboratory experiments show that turbulent environments drive small scale patches in motile phytoplankton. As the numerical studies predicted, motility substantially decreases the distance between neighbouring cells, altering the topology of their distribution. Patchiness generated by motility-driven unmixing may have multitude of consequences for phytoplankton. On the one hand, heterogeneous distribution may have advantages during the reproduction times, as it reduces the distance between conspecific cells. On the other hand, patchiness could be detrimental sharpening the nutrients competition. Furthermore, laser exposure does not have any effect on Phytoplankton's behavior, whereas turbulence exposure disorientates the cells, making them slower within the flow. It has been also observed that the cells recover their original behavior over time. Indeed, the turbulence effects on Phytoplankton cells are temporary rather than permanent.

The results obtained have a great relevance to the research studies of microorganism distribution under turbulence conditions. In fact, this project has been used for writing and submitting a proposal for grant to the National Science Foundation (NSF). The grant would allow to perform a new set of experiments in a 3D turbulence tank that mimics, in a more realistic way, the oceanic flow conditions.

References

Bearon, R. (2000). Helical swimming can provide robust upwards transport for gravitactic single-cell algae; a mechanistic model. *Journal of Mathematical Biology*.

Crimaldi, J. (2008). Planar laser induced fluorescence in aqueous flows. *Experiments in Fluids*, 44(6):851–863.

Durham, W., Climent, E., Barry, M., De Lillo, F., Boffetta, G., Cencini, M., and Stocker, R. (2013). Turbulence drives microscale patches of motile phytoplankton. *Nature Communications*, (4)2148.

Durham, W., Climent, E., and Stocker, R. (2011). Gyrotaxis in a steady vortical flow. *Physical Review Letters*, 106(23):238102.

Grant, I. (1997). Particle image velocimetry: a review. *Proceedings of the Institution of Mechanical Engineers, Part C:Journal of Mechanical Engineering Science*, 211(1):55–76.

Hara, Y. and Chihara, M. (1987). Morphology, ultrastructure and taxonomy of the raphidophycean alga *Heterosigma akashiwo*. *The botanical magazine*, 100:151–163.

Hedrick, T. (2008). Software techniques for two- and three-dimensional kinematic measurements of biological and biomimetic systems. *Bioinspiration and Biomimetics*, 3.

Hinze, J. (1975). *Turbulence*. McGraw-Hill, New York.

Leeuw, T., Boss, E., and Wright, D. (2013). *In situ* measurements of phytoplankton fluorescence using low cost electronics. *Sensors*, 13:7872–7883.

Pedley, T. and Kessler, J. (1992). Hydrodynamic phenomena in suspensions of swimming microorganisms. *Annual Review Fluid Mechanics*, 24:313–358.

Peters, F. and Redondo, J. (1997). Turbulence generation and measurement: application to studies on plankton. *Scientia Marina*, 61(S1):205–228.

Saarenrinne, P. and Piirto, M. (2000). Turbulent kinetic energy dissipation rate estimation from piv velocity vector fields. *Experiments in Fluids*, pages 300–307.

Soltys, M. and Crimaldi, J. (2011). Scalar interactions between parallel jets measured using a two channel plif technique. *Experiments in Fluids*, 50(6):151–163.

Srdic, A., Fernando, H., and Montenegro, L. (1996). Generation of nearly isotropic turbulence using two oscillating grids. *Experiments in Fluids*, 20(5):395–397.

Westerweel, J., G.E., E., and R.J., A. (2012). Particle image velocimetry for complex and turbulent flows. *The Annual Review of Fluid Mechanics*, 45:409–436.

Willert, C. and Gharib, M. (1991). Digital particle image velocimetry. *Experiments in Fluids*, 10:181–193.